SCIENCE CHINA
Information Sciences

• LETTER •

October 2026, Vol. 69, Iss. 10, 209301:1–209301:2
https://doi.org/10.1007/s11432-025-4801-2

Enhanced imaging of synthetic aperture interferometric radiometer via spatial domain gradient characteristic analysis

Xinpeng CHEN[1], Dong ZHU[1,2*], Bo FANG[1], Jingyu TAO[1] & Fei HU[1,2]

[1] *School of Electronic Information and Communications, Huazhong University of Science and Technology, Wuhan 430074, China*
[2] *National Key Laboratory of Science and Technology on Multi-Spectral Information Processing, Wuhan 430074, China*

Received 15 May 2025/Revised 16 December 2025/Accepted 10 February 2026/Published online 28 August 2026

Citation Chen X P, Zhu D, Fang B, et al. Enhanced imaging of synthetic aperture interferometric radiometer via spatial domain gradient characteristic analysis. Sci China Inf Sci, 2026, 69(10): 209301, https://doi.org/10.1007/s11432-025-4801-2

This study focuses on the synthetic aperture interferometric radiometer (SAIR), a high-resolution imaging technology that synthesizes an equivalent large aperture through antenna arrays [1]. It has been widely applied in fields such as remote sensing, atmospheric sounding, weather forecasting, ocean observation, and security inspection. For instance, the European Space Agency's SMOS mission and NASA's CYGNSS project have successfully employed SAIR for monitoring soil moisture, ocean salinity, and tropical cyclones, demonstrating its significant value in global environmental and climate studies.

However, the imaging quality of conventional SAIR implementations is frequently compromised by noise contamination and diffraction artifacts [2]. Reconstructing brightness temperature (BT) images from sparse and noisy visibility samples constitutes a severely ill-posed inverse problem, which is also prevalent in fields such as radar [3]. Traditional Fourier-based inversion methods, while computationally efficient, are prone to grating lobes and edge artifacts. Existing regularization approaches, such as Tikhonov and compressed sensing (CS), partially mitigate the ill-posedness but often struggle to balance noise suppression with the preservation of structural features, frequently overlooking the spatial domain gradient structure and local correlations of the target. In recent years, deep learning-based methods have shown remarkable feature extraction capabilities, yet their "black-box" nature limits interpretability, and their generalization remains constrained in practical scenarios with scarce training data or distribution changes.

Therefore, achieving high-quality SAIR imaging under strong noise interference has become a critical scientific problem to be solved. From a novel perspective of spatial domain gradient characteristics, this study presents a spatial domain gradient-constrained imaging framework to address the limitations of existing methods through three principal contributions. First, a systematic analysis of the spatial domain gradient distribution of SAIR targets reveals a hyper-Laplacian (HL) prior governing spatial domain characteristics. Second, we develop an overlapping group sparse (OGS) regularization technique incorporating this prior, which effectively exploits both inter-pixel correlations and gradient sparsity. Third, an optimization framework combining the alternating direction method of multipliers (ADMM) with majorization-minimization (MM) algorithms is formulated, where a novel quadratic substitution strategy is introduced to resolve the non-convex Lq quasi-norm minimization problem. Comprehensive validation through simulations and real-scene experiments demonstrates that the proposed framework significantly outperforms conventional interferometric radiometry imaging methods in quantitative metrics assessments, exhibiting excellent noise suppression and structural preservation capabilities. This work not only advances the theoretical development of SAIR imaging, but also provides effective technical support for high-precision remote sensing applications such as military reconnaissance, polar exploration, and disaster monitoring.

Fundamental principles of SAIR. The mathematical correspondence between the acquired visibility measurements and the modified BT distribution is governed by the following integral formulation [4]:

$$\mathcal{V}(u_{ik}, v_{ik}) = \iint_{l^2+m^2\leqslant 1} T_M(l,m) e^{-j2\pi(u_{ik}l+v_{ik}m)} dl dm \quad (1)$$

with

$$\begin{aligned} T_M(l,m) = {} & \frac{\sqrt{D_i D_k}}{4\pi} \frac{T_B(l,m) - T_r}{\sqrt{1-l^2-m^2}} \cdot f_i(l,m) \\ & \cdot f_k^*(l,m) \phi_{ik}\left(-\frac{u_{ik}l + v_{ik}m}{f_c}\right), \end{aligned} \quad (2)$$

where $T_M(l,m)$ represents the modified BT. Here, D_i and D_k correspond to the maximum directivity of antenna i and k, respectively, and their normalized voltage radiation patterns are represented by $f_i(l,m)$ and $f_k(l,m)$. ϕ_{ik} is the fringe-washing function. T_r stands for the receiver's physical temperature, while f_c indicates the correlation receiver's central frequency. In the spherical coordinate system, the direction cosines are denoted by $l = \sin\theta\cos\varphi$ and $m = \sin\theta\sin\varphi$. (u_{ik}, v_{ik}) is the u-v baseline between the i-th and k-th antennas, which is expressed as follows:

$$(u_{ik}, v_{ik}) = \left(\frac{x_k - x_i}{\lambda_c}, \frac{y_k - y_i}{\lambda_c}\right), \quad (3)$$

* Corresponding author (email: dzhu@hust.edu.cn)

where (x_i, y_i) and (x_k, y_k) are the Cartesian coordinates of the antenna i and k, respectively. λ_c is the center wavelength. In the spatial frequency domain, the distribution of u-v baselines corresponds to a set of discrete sampling points, which exhibit symmetry centered at the origin. The spacing between these sampling points is directly related to the field of view (FOV) of alias-free imaging, while the maximum baseline length determines the highest spatial frequency that the system can sample.

In the problem of SAIR image reconstruction, our objective is to reconstruct a spatial-domain BT map from frequency-domain visibility samples. According to the Nyquist sampling criterion, the SAIR sampling problem can be formulated as

$$\mathbf{V} = \mathbf{G}\mathbf{T} + \mathbf{n}, \tag{4}$$

where $\mathbf{V}^{p\times 1}$ represents the visibility vector obtained through SAIR sampling in the spatial frequency domain. $\mathbf{T}^{q\times 1}$ denotes the BT distribution of the observed scene. $\mathbf{G}^{p\times q}$ is the system model operator of SAIR, characterizing the system response that transforms the input BT distribution into the output visibility function. $\mathbf{n}$ represents the noise in the visibility during the acquisition process, which approximately follows a Gaussian distribution.

HL prior criterion. The probability density function associated with the HL distribution can be expressed as [5]

$$P(x|\alpha, q) = \frac{q}{2}\left(\frac{\alpha}{2}\right)^{\frac{1}{q}} e^{\left(-\frac{\alpha}{2}|x-\mu|^q\right)} / \Gamma\left(\frac{1}{q}\right), \tag{5}$$

where x represents the gradient of a pixel. μ is the expected value. $\Gamma(\cdot)$ denotes the Gamma function. The parameter α governs the width of the function, while q regulates its amplitude. Specifically, q acts as the HL parameter, constrained to the interval $[0.5, 1]$.

To verify that the spatial gradients of SAIR images follow an HL distribution, we conducted a statistical analysis of the probability density distribution of the SAIR spatial domain gradient in this dataset. The datasets cover various scenes including agriculture, beaches, jungles, buildings, lakes, and parked aircraft at airports. As shown in Figure 1(a), we plotted fitting curves as empirical first-order gradient distributions. The empirical first-order distributions were generated by averaging the histograms of SAIR images in the form of probability density (deep blue), along with fitted Gaussian (light orange), Laplacian (green), and HL (deep red) distributions. Through examination of the results, we conclude that the empirical distribution can be well approximated by the HL distribution, whereas both Gaussian and Laplacian distributions exhibit significant fitting errors.

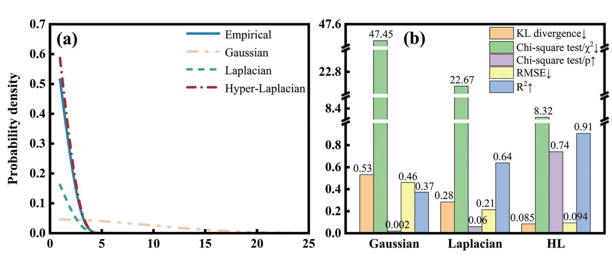

Figure 1 (Color online) (a) Statistical results and (b) quantitative statistical measures of the gradient probability density distribution in the SAIR spatial domain.

Furthermore, we supplemented quantitative statistical measures (as shown in Figure 1(b)), including the KL divergence, Chi-square test χ^2 and p-value, RMSE, and R^2. These metrics consistently and clearly demonstrate across multiple dimensions that among the Gaussian, Laplacian, and HL distributions, the HL distribution exhibits the best fit to the SAIR spatial domain gradient distribution. Such goodness-of-fit metrics substantially strengthen the confidence in our conclusions.

Proposed SAIR imaging framework. In contrast to previous works, the proposed framework explicitly accounts for overlapping groups in spatial domain gradients, thereby better preserving local structural information of the target. Given that the spatial domain gradient distribution of the SAIR targets follows the HL distribution, we formulate an optimization problem as follows:

$$\begin{aligned} &\min_{\mathbf{T},\mathbf{Y}_1,\mathbf{Y}_2} \left\{ \frac{1}{2}\|\mathbf{V} - \mathbf{D}\mathbf{T}\|_2^2 + \lambda\left[\varphi_{\mathrm{OH}}(\mathbf{Y}_1) + \varphi_{\mathrm{OH}}(\mathbf{Y}_2)\right] \right\} \\ &\text{s.t. } \mathbf{Y}_1 = \nabla_x \mathcal{R}(\mathbf{T}),\ \mathbf{Y}_2 = \nabla_y \mathcal{R}(\mathbf{T}), \end{aligned} \tag{6}$$

where λ is the regularization parameter, and $\mathbf{G}$ is set as $\mathbf{D}$, with $\mathbf{D}$ representing the Fourier transform operator. $\varphi_{\mathrm{OH}}(\cdot)$ denotes the OGSHL regularization term, and $\mathbf{Y}_1, \mathbf{Y}_2 \in \mathbb{R}^{K\times K}$ are two auxiliary variables. ∇_x and ∇_y represent the spatial gradient operators along horizontal and vertical axes, and $\mathcal{R}(\cdot): \mathbb{R}^Q \to \mathbb{R}^{K\times K}$ operator to represent the linear mapping relationship. The problem above can be solved by ADMM, within which the subproblems involving overlapping structures were iteratively solved under the MM algorithmic framework. The detailed steps are provided in Appendix A.

Appendix B presents simulation and real-scene imaging results under various noise levels, fully validating the performance and robustness of the proposed algorithm. Appendix C provides a systematic analysis of the algorithm's performance, including sensitivity to HL parameters, adaptive selection strategies, algorithmic complexity, and potential acceleration strategies. Together, these results highlight the algorithm's practical utility and significance.

Conclusion. This study introduces an OGSHL imaging framework based on spatial domain gradient information to mitigate noise interference in SAIRs, restore structural details of reconstruction targets, and thereby improve imaging quality. First, we conducted a statistical analysis of the probability density distribution of SAIR spatial domain gradients, revealing that the empirical distribution aligns more closely with the HL prior. Second, leveraging this characteristic, we innovatively integrate OGS regularization with the HL prior. By exploiting structurally sparse patterns in the spatial domain, the proposed framework effectively captures local correlation features of the data, enabling high-quality reconstruction of SAIR targets. Finally, simulation and real data results validate the efficacy of the proposed imaging framework in suppressing noise interference and improving imaging quality.

Acknowledgements This work was supported by National Natural Science Foundation of China (Grant No. 62271219) and Fundamental Research Funds for the Central Universities (Huazhong University of Science and Technology), China.

Supporting information Appendixes A–C. The supporting information is available online at info.scichina.com and link.springer.com. The supporting materials are published as submitted, without typesetting or editing. The responsibility for scientific accuracy and content remains entirely with the authors.

References

1 Xu Y, Zhu D, Hu F, et al. Rfi localization using jointly nonconvex low-rank approximation and expanded virtual array in microwave interferometric radiometry. IEEE Trans Geosci Remote Sens, 2023, 61: 5300515
2 Zhang Y, Ren Y, Miao W, et al. Microwave SAIR imaging approach based on deep convolutional neural network. IEEE Trans Geosci Remote Sens, 2019, 57: 10376–10389
3 Wang W W, Wang Z M, Yuan Z Y, et al. A fast and adaptive method for complex-valued SAR image denoising based on l k norm regularization. Sci China Ser F-Inf Sci, 2009, 52: 138–148
4 Zhu D, Lu H, Cheng Y. Rfi source detection based on reweighted ℓ_1-norm minimization for microwave interferometric radiometry. IEEE Trans Geosci Remote Sens, 2022, 60: 5301415
5 Deng L J, Feng M, Tai X C. The fusion of panchromatic and multispectral remote sensing images via tensor-based sparse modeling and hyper-Laplacian prior. Inf Fusion, 2019, 52: 76–89